mater.scichina.com link.springer.com

Published online 17 January 2023 | https://doi.org/10.1007/s40843-022-2297-1
Sci China Mater 2023, 66(5): 1870–1878

Large-area epitaxial growth of 2D $ZrS_{2(1-x)}Se_{2x}$ semiconductor alloys with fully tunable compositions and bandgaps for optoelectronics

Jidong Huang[1,2], Yan Tian[1,2], Yong Cheng[1,2], Xingxing Li[3*], Siyu Zhang[1,2], Ji Jiang[1,2], Jingren Chen[1,2], Gaokai Wang[1,2], Jingzhen Li[1,2], Zhigang Yin[1,2] and Xingwang Zhang[1,2,3*]

ABSTRACT **Bandgap engineering of transition metal dichalcogenides (TMDs) is significant for broadening their applications in electronics and optoelectronics devices. Herein, we report the new epitaxial growth of large-area uniform $ZrS_{2(1-x)}Se_{2x}$ alloy films with fully tunable composition on sapphire substrates *via* a facile single-step chemical vapor deposition method. The $ZrS_{2(1-x)}Se_{2x}$ alloys exhibit good single crystallinity and epitaxial quality, as well as uniform elemental distribution, and the epitaxial relationship with the substrate is determined to be $ZrS_{2(1-x)}Se_{2x}$ (0001)[10-10]||sapphire (0001)[11-20]. The bandgap of $ZrS_{2(1-x)}Se_{2x}$ alloy exhibits a pronounced bowing behavior with continuously tunable bandgaps from 1.86 to 1.15 eV, depending on the Se composition. The $ZrS_{2(1-x)}Se_{2x}$-based photodetectors demonstrate a sensitive photoresponse to visible light with a fast response time of ~100 μs, and their performances are significantly improved as the Se composition decreases. This work provides an efficient way to synthesize $ZrS_{2(1-x)}Se_{2x}$ alloys with fully tunable bandgaps, providing great flexibility in designing TMD-based optoelectronic devices.**

Keywords: transition metal dichalcogenides, alloying, photodetectors, epitaxial growth, chemical vapor deposition

INTRODUCTION

Layered two-dimensional (2D) transition metal dichalcogenides (TMDs) have attracted considerable interest due to their layered structures, excellent optical and electrical properties, and enormous potential applications [1–4]. Unlike graphene with a zero bandgap, most 2D TMDs possess a semiconducting band structure and a thickness-dependent bandgap, which are essential for electronic and optoelectronic applications. However, the fixed bandgap value of binary TMDs seriously limits the scope of their potential applications. Bandgap engineering is an important strategy to provide great flexibility in tailoring the bandgap of TMD materials and broaden their applications significantly. Due to atomic structural similarities, alloying has been proven effective in enabling bandgap engineering by tuning the chemical composition of 2D TMDs. To date, several 2D TMD alloys with tunable bandgaps and carrier types have been prepared by various methods, including chemical vapor transport (CVT), chemical vapor deposition (CVD), and molecular beam epitaxy [5,6]. Nevertheless, currently most reports focus on group-VIB TMDs, such as $MoS_{2(1-x)}Se_{2x}$ [7–9], $WS_{2(1-x)}Se_{2x}$ [10–12], $MoTe_{2(1-x)}Se_{2x}$ [13], $WSe_{2(1-x)}Te_{2x}$ [14], $Mo_{1-x}W_xS_2$ [15–18], and $Mo_{1-x}W_xSe_2$ [19], as well as other TMD alloys including $ReS_{2(1-x)}Se_{2x}$ [20,21], $W_{1-x}Re_xS_2$ [22], $Nb_{1-x}W_xSe_2$ [23], and $MoS_{2(1-x-y)}Se_{2x}Te_{2y}$ [24].

Recently, group-IVB TMDs have gained more attention due to their theoretically predicted high acoustic-phonon-limited mobilities and sheet current densities [25–27]. For example, ZrS_2 and $ZrSe_2$ have been calculated to have an acoustic-phonon-limited room-temperature mobility of 1247 and 2316 $cm^2 V^{-1} s^{-1}$, respectively, which are nearly an order of magnitude higher than those of widely studied MoS_2 (340 $cm^2 V^{-1} s^{-1}$) [26]. Additionally, the calculated sheet current densities of $ZrSe_2$- and ZrS_2-based tunneling field-effect transistors are ~6000 and 800 μA $μm^{-1}$, respectively, which also significantly exceed those of group-VIB TMDs [27]. Despite these predicted outstanding theoretical electronic properties, alloying based on group-IVB TMDs is seldom reported. Recently, $ZrS_{2(1-x)}Se_{2x}$ alloy flakes have been synthesized by the CVT method [28–30], and few-layer $ZrS_{2(1-x)}Se_{2x}$ nanosheets can then be achieved by mechanical exfoliation. However, the limited size of exfoliated 2D nanosheets makes them unsuitable for large-area electronic applications. Hence, the large-area growth of ternary TMD alloys with tunable bandgaps is significant for broad device applications. CVD is a popular route for large-scale and low-cost synthesis of 2D TMDs because of its simplicity, repeatability, and scalability. In fact, large-area $HfS_{2(1-x)}Se_{2x}$ alloys have been directly synthesized by a low-pressure CVD method [31]. However, to the best of our knowledge, the large-area growth of 2D $ZrS_{2(1-x)}Se_{2x}$ ternary alloys has not been realized to date.

Herein, the novel epitaxial growth of large-area $ZrS_{2(1-x)}Se_{2x}$ alloys with fully tunable compositions is achieved on *c*-plane sapphire substrates *via* a one-step CVD method using $ZrCl_4$, Se, and S powders as reactants. The crystalline quality and epitaxial relations of the $ZrS_{2(1-x)}Se_{2x}$ alloys are systematically characterized by various techniques. The lattice constant (*c*) of layered $ZrS_{2(1-x)}Se_{2x}$ alloys linearly increases as the Se composition increases, consistent with Vegard's law. The bandgap of $ZrS_{2(1-x)}Se_{2x}$ alloys demonstrates a pronounced bowing effect with a continuously tunable value from 1.86 to 1.15 eV. Besides, the density functional theory (DFT) calculations show a similar

[1] Key Lab of Semiconductor Materials Science, Institute of Semiconductors, Chinese Academy of Sciences, Beijing 100083, China
[2] Center of Materials Science and Optoelectronics Engineering, University of Chinese Academy of Sciences, Beijing 100049, China
[3] Joint Lab of Digital Optical Chip, Wuyi University, Jiangmen 529020, China
* Corresponding authors (emails: wyuxxli@163.com (Li X); xwzhang@semi.ac.cn (Zhang X))

 © Science China Press 2023

dependence of bandgap on Se composition. Additionally, several photodetectors were fabricated based on the $ZrS_{2(1-x)}Se_{2x}$ alloys. The $ZrS_{2(1-x)}Se_{2x}$ photodetectors exhibit excellent comprehensive performance and different spectral response bands depending on their compositions. The synthesis of $ZrS_{2(1-x)}Se_{2x}$ alloys with fully tunable bandgaps provides great flexibility in designing TMD-based optoelectronic devices.

EXPERIMENTAL SECTION

Synthesis of $ZrS_{2(1-x)}Se_{2x}$ alloy films

The $ZrS_{2(1-x)}Se_{2x}$ alloys were synthesized on the *c*-plane sapphire substrates by a low-pressure CVD system with two independent heating zones. S (>99.9995%, Alfa Aesar), Se (>99.999%, Alfa Aesar), and $ZrCl_4$ (>99.9%, Aladdin) powders were successively placed at heating zone I (the upstream of the tube reactor) as solid-state reaction sources, and the cleaned *c*-plane sapphire was located in heating zone II (the downstream of the tube reactor) as the substrate. Their respective positions are illustrated in Fig. S1. The mass of $ZrCl_4$ powders was 50 mg, and the alloy composition was adjusted by varying the mass ratio of the S and Se powders, with their total masses being constant at 1 g. The temperatures in heating zones I and II were set to 350 and 1000°C, respectively. Before heating, the quartz tube was firstly pre-evacuated down to a base pressure of 5 Pa and backfilled with Ar to a working pressure of 50 Pa. Finally, the $ZrS_{2(1-x)}Se_{2x}$ alloy films were grown under a mixed carrier gas of Ar (20 sccm (standard cubic centimeter per minute)) and H_2 (10 sccm) for 5–10 min. The resulting film thickness was ~10–20 nm, as determined by the step profiler.

Characterizations

Optical photographs of the $ZrS_{2(1-x)}Se_{2x}$ alloys were taken on an Olympus BX51M microscope. The microstructure of the layered $ZrS_{2(1-x)}Se_{2x}$ was characterized by transmission electron microscopy (TEM, JEOL JEM-2010, 120 kV) equipped with energy dispersive X-ray spectroscopy (EDS). The compositions of the alloys were analyzed by X-ray photoelectron spectroscopy (XPS, Thermo Scientific, ESCALAB250-Xi) with 1486.6 eV Al Kα radiation as the excitation source. Raman spectra were performed using a SmartRaman confocal-micro-Raman module with a 532-nm laser excitation at room temperature. X-ray diffraction (XRD) spectra were recorded by a Rigaku D/MAX-2500 system using Cu Kα as the X-ray source. Ultraviolet-visible light (UV-Vis) absorption spectra were acquired using a Varian Cary 5000 spectrophotometer in the double-beam mode.

Computational methods

The electronic band structures, total density of states (TDOS), and partial density of states (PDOS) of the $ZrS_{2(1-x)}Se_{2x}$ alloys were calculated by DFT with the projector-augmented wave pseudopotential as implemented in the Vienna *Ab initio* Simulation Package. With the investigated experimental cell, the energy cut-off was 350 eV, and the Monkhorst-Pack *k*-point sampling in the Brillouin zone was *Γ*-centered with 5 × 5 × 3 in all calculations. The electronic band structure calculations were performed using the generalized gradient approximation in the parametrization by the Perdew-Burke-Ernzerhof (PBE). Supercells comprising 2 × 2 × 2 unit cells were constructed to simulate $ZrS_{2(1-x)}Se_{2x}$ alloys with different Se compositions (*x*). For each specified *x*-value, S atoms were randomly replaced by Se atoms. All $ZrS_{2(1-x)}Se_{2x}$ structures were initially relaxed until the force per atom was <0.01 eV $Å^{-1}$, and the convergence criterion for the total energy was taken as $<10^{-6}$ eV.

Device fabrication and measurements

The photodetectors were fabricated by depositing two 200-nm-thick Au electrodes with a 20-μm interval by thermal evaporation on the $ZrS_{2(1-x)}Se_{2x}$ films grown on the sapphire substrates. The current-voltage (*I*-*V*) characteristics, the response time, and the photocurrent mapping were measured with a scanning photoelectric test system (MStarter-200). A 405-nm laser was used as the light source since all the $ZrS_{2(1-x)}Se_{2x}$-based detectors show high photoresponse within the wavelength range of 400–450 nm. The spot size of a focused single-mode laser was ~1 μm for the measurements of photocurrent mapping. The 405-nm multimode laser was modulated at 250 Hz to measure the response time by a signal generator. The spectral photoresponse curves were acquired by an Andor Kymera 328i spectrometer using a xenon lamp (Hamamatsu) and monochromator (Omni-λ 200i) combination.

RESULTS AND DISCUSSION

The synthesis of ternary $ZrS_{2(1-x)}Se_{2x}$ alloys was performed in a two-temperature zone tube furnace. As schematically illustrated in Fig. S1, S, Se, and $ZrCl_4$ powders were placed in three quartz boats in the heating zone I, respectively, and the sapphire substrate was placed in the center of heating zone II located downstream of the quartz tube. The Ar/H_2 mixture with a flow rate of 20/10 sccm was used as the carrier gas. The substrate temperature was typically kept at 1000°C, and the growth time was 5–10 min.

Several $ZrS_{2(1-x)}Se_{2x}$ alloy films with continuously tunable compositions (x = 0–1) were synthesized on *c*-plane sapphire substrates by systematically adjusting the mass ratio of S and Se powders. A typical full XPS spectrum of the as-grown $ZrS_{2(1-x)}Se_{2x}$ alloy is shown in Fig. S2, from which the predominant XPS signals of Se, S, and Zr are clearly seen along with weak C and Al signals from surface contamination and the sapphire substrate. The Se 3p and S 2p XPS core-level spectra of $ZrS_{2(1-x)}Se_{2x}$ alloys with different Se compositions are shown in Fig. 1a. Apparently, the intensities of the S $2p_{3/2}$ (161.0 eV) and S $2p_{1/2}$ peaks (162.2 eV) decrease monotonically as the Se composition increases, whereas the Se $3p_{3/2}$ (159.8 eV) and Se $3p_{1/2}$ (165.4 eV) peaks appear and gradually increase as the Se composition increases. The composition *x* of each $ZrS_{2(1-x)}Se_{2x}$ alloy (Fig. 1a) was obtained by normalizing the integrated intensities of the S 2p and Se 3p peaks to the corresponding sensitivity factors.

The structures of $ZrS_{2(1-x)}Se_{2x}$ alloys with different Se compositions were investigated by XRD. As shown in Fig. 1b, apart from the (0006) reflection of the sapphire substrate, only strong (000*l*) reflections of 1T-$ZrS_{2(1-x)}Se_{2x}$ are clearly observed for all samples, implying that the $ZrS_{2(1-x)}Se_{2x}$ films are highly *c*-axis oriented. We take a closer look at Fig. 1c by zooming in on Fig. 1b with a focus on the (0001) reflections of alloys. Obviously, the (0001) diffraction peak of $ZrS_{2(1-x)}Se_{2x}$ slightly shifts toward lower 2θ angles as the Se composition increases. According to Bragg's equation, *c* is calculated from the XRD patterns, which exhibits a nearly linear relationship with *x* (Fig. S3). Such a composition dependence of *c* is consistent with the well-known Vegard's law, providing a quick method to precisely determine the composition of $ZrS_{2(1-x)}Se_{2x}$ alloys. The

© Science China Press 2023

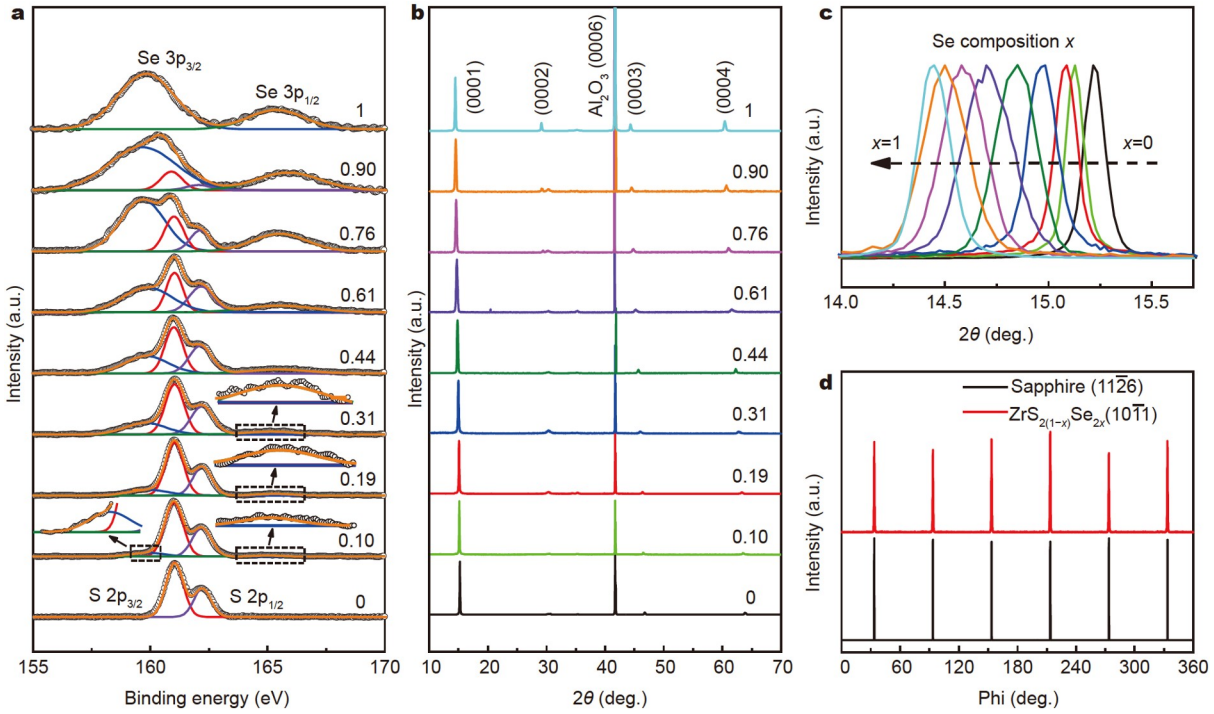

Figure 1 (a) Normalized Se 3p/S 2p core-level XPS spectra and (b) XRD θ-2θ patterns of $ZrS_{2(1-x)}Se_{2x}$ alloys with different Se compositions. (c) Zoomed-in view of the (0001) reflection of $ZrS_{2(1-x)}Se_{2x}$ alloys in (b), showing an obvious shift toward lower angles with Se composition increasing. (d) Phi-scans XRD spectra of $ZrS_{2(1-x)}Se_{2x}$ (10-11) and sapphire (11-26) reflections.

full width at half maximum of the X-ray rocking curve is ~41 arcmin for a typical $ZrS_{2(1-x)}Se_{2x}$ alloy (Fig. S4), which is comparable to that of ZrS_2 and $ZrSe_2$ [32,33]. The phi-scan XRD spectra for the $ZrS_{2(1-x)}Se_{2x}$ (10-11) and sapphire (11-26) reflections are shown in Fig. 1d. Both spectra show six well-defined diffraction peaks separated by 60° at the same azimuthal angles. Combining the XRD θ-2θ scans with the phi-scans, the epitaxial relationship between the $ZrS_{2(1-x)}Se_{2x}$ alloy and the sapphire substrate was determined as $ZrS_{2(1-x)}Se_{2x}$ (0001)[10-10]||sapphire (0001)[11-20].

Raman measurements were conducted at room temperature to evaluate the composition-dependent vibration modes of the $ZrS_{2(1-x)}Se_{2x}$ alloys. Fig. 2a presents the normalized Raman spectra of the as-grown $ZrS_{2(1-x)}Se_{2x}$ alloys with x varying from 0 (pure ZrS_2) to 1 (pure $ZrSe_2$). The dominant feature in the Raman spectrum of the ZrS_2 film is a broad asymmetric peak located at ~330 cm^{-1}, which is ascribed to the out-of-plane $A_{1g}^{S\text{-}Zr}$ mode at 332 cm^{-1} along with the infrared mode $A_{2u}^{S\text{-}Zr}$ at ~320 cm^{-1} activated by long-range Coulomb forces [33–35]. Besides, the weak peak at 247 cm^{-1} originates from the in-plane $E_g^{S\text{-}Zr}$ mode of ZrS_2. In contrast, the $ZrSe_2$ film exhibits two Raman characteristics modes, i.e., the strong and weak peaks located at ~192 and 258 cm^{-1}, which are assigned to the out-of-plane vibration of the Se atoms ($A_{1g}^{Se\text{-}Zr}$ mode) and the Coulomb-force-activated infrared mode $A_{2u}^{Se\text{-}Zr}$, respectively [28,29,32,35]. For the $ZrS_{2(1-x)}Se_{2x}$ alloys, the Zr-S-related Raman peaks gradually decrease in intensity and finally disappear as x increases. Meanwhile, the Se-Zr-related modes appear and gradually prevail. In addition to the peak intensity variation, the positions of most vibrational modes exhibit apparent redshifts as x increases (Fig. 2b), which is attributed to the larger reduced mass of the $ZrS_{2(1-x)}Se_{2x}$ alloys with a higher x-value [36]. The observed Raman shifts and intensity change agree excellently with those of the mechanical exfoliated $ZrS_{2(1-x)}Se_{2x}$ alloys [28,29], confirming the expected structural and compositional evolution in the $ZrS_{2(1-x)}Se_{2x}$ alloys. Interestingly, two additional Raman peaks are clearly observed at 201 and 220 cm^{-1} for the ternary $ZrS_{2(1-x)}Se_{2x}$ alloys, which are labeled as D_1 and D_2 in Fig. 2a, b, respectively. Close examination of Fig. 2a shows that the intensity of the D_2 peak increases initially and decreases as x increases, and it becomes the dominant feature for the $ZrS_{2(1-x)}Se_{2x}$ alloys with middle Se composition ($0.31 \leq x \leq 0.61$), indicating that these modes are related to the alloying effect of S and Se. This alloy-induced activation of disorder modes is attributed to the different configurations of S and Se atoms around Zr atoms, which was also observed for the CVT-grown $ZrS_{2(1-x)}Se_{2x}$ nanosheets [28]. Furthermore, the optical microscopy and Raman mapping images show that morphology and composition are very uniform for the $ZrS_{2(1-x)}Se_{2x}$ alloy film (Fig. S5).

Fig. 2c shows the optical photographs of the $ZrS_{2(1-x)}Se_{2x}$ films with different x-values. All the $ZrS_{2(1-x)}Se_{2x}$ films exhibit uniform color distribution, suggesting good surface morphology and uniform thickness. Especially, the colors of $ZrS_{2(1-x)}Se_{2x}$ films with the lower x-values are yellow or light brown and gradually deepen as x increases. The color change of the alloys reflects the bandgap variation with composition. To precisely determine the bandgap values of the $ZrS_{2(1-x)}Se_{2x}$ alloys, their UV-Vis absorption spectra were measured. As shown in Fig. 2d, the absorption edge of the $ZrS_{2(1-x)}Se_{2x}$ alloys generally shifts toward higher wavelengths as x increases, indicating that the bandgap decreases as x increases. As an indirect bandgap semiconductor, the

© Science China Press 2023

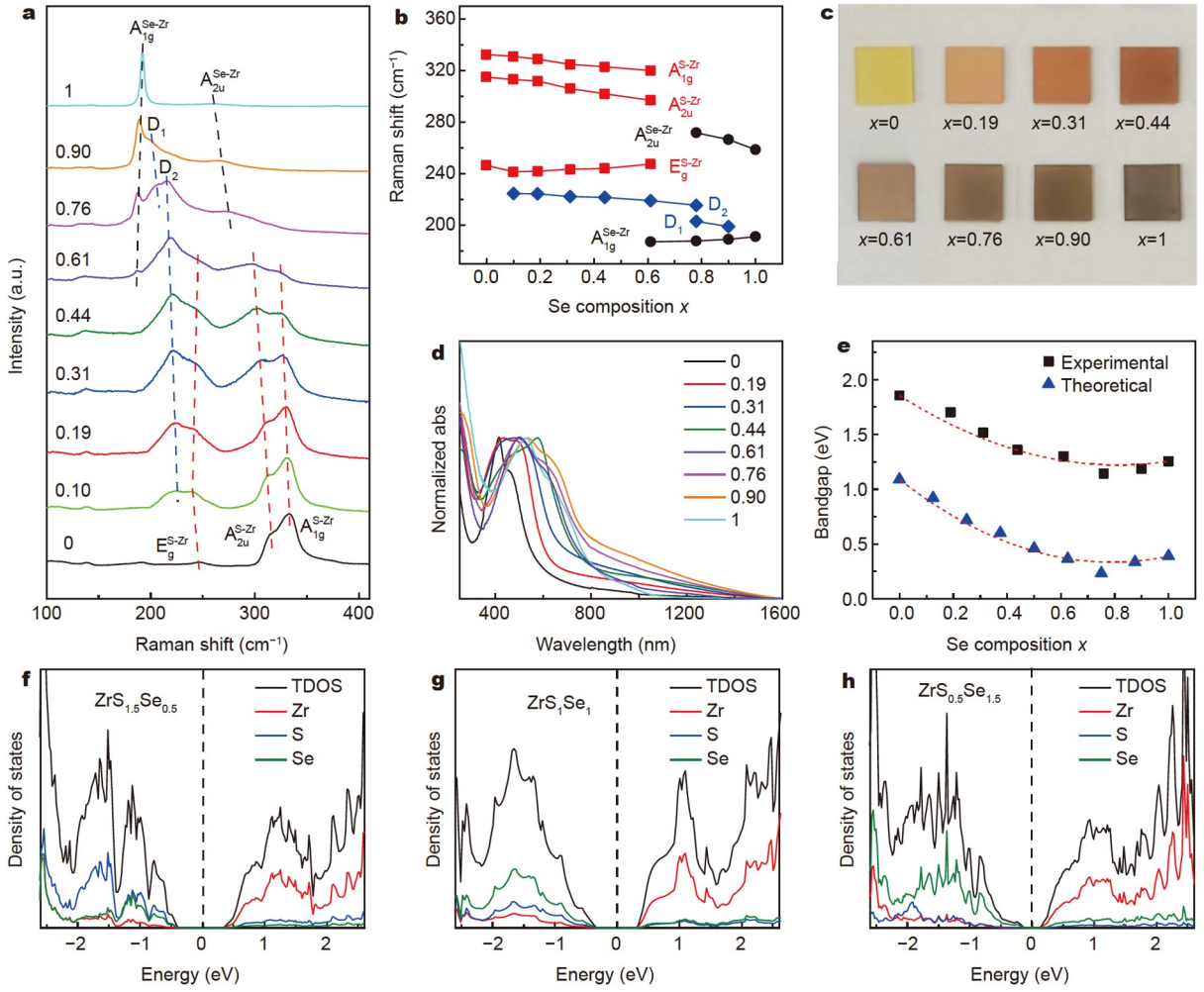

Figure 2 (a) Normalized Raman spectra of $ZrS_{2(1-x)}Se_{2x}$ alloys with different Se compositions (x). (b) Plots of Raman peak position as a function of the Se composition (x) for seven primary Raman modes. (c) Optical photographs and (d) normalized UV-Vis absorption spectra of $ZrS_{2(1-x)}Se_{2x}$ alloys with different Se compositions (x). (e) Plots of the experimental and theoretical bandgap of $ZrS_{2(1-x)}Se_{2x}$ alloys as a function of the Se composition (x). Dashed lines show least-square fitting results. The DFT-calculated TDOS and PDOS projected on specific Zr, S, or Se atoms for (f) $ZrS_{1.5}Se_{0.5}$, (g) ZrS_1Se_1, and (h) $ZrS_{0.5}Se_{1.5}$ alloys.

bandgap can be determined by fitting the extrapolating linear region of Tauc's plot $[(\alpha h\nu)^{1/2}$ *vs.* $(h\nu)]$, where α is the absorption coefficient, and $h\nu$ is the photon energy (Fig. S6). In Fig. 2e, the obtained bandgap is plotted as a function of x. Interestingly, the bandgap exhibits an obvious bowing effect as x varies. As x increases from 0 to 1, the bandgap (E_g) initially decreases from 1.86 to 1.15 eV. Afterward, it gradually increases to 1.26 eV. Specifically, the bowing effect can be described as follows:

$$E_g^{ZrS_{2(1-x)}Se_{2x}} = (1-x)E_g^{ZrS_2} + xE_g^{ZrSe_2} - bx(1-x). \quad (1)$$

The bowing parameter b is extracted to be 0.96 eV by fitting the experimental data into Equation (1) (Fig. 2e). For most ternary TMD alloys, the bandgap varies linearly *versus* the composition [7,10,11,31]. Nevertheless, the bowing effect has also been reported for some ternary TMD alloys, such as $Mo_{1-x}W_xS_2$ [15,18,37] and $ReS_{2x}Se_{2(1-x)}$ [20]. To confirm the observed bowing effect, the electronic band structures of the $ZrS_{2(1-x)}Se_{2x}$ alloys with different compositions were calculated using the DFT within the PBE hybrid functional. The results indicate that the $ZrS_{2(1-x)}Se_{2x}$ alloys are indirect bandgap semiconductors with the valence band maximum at Γ and the conduction band minimum at L (Fig. S7), which is consistent with the previous results [38,39]. Because the PBE method is well known to underestimate the bandgap [40], the calculated bandgaps of $ZrS_{2(1-x)}Se_{2x}$ are significantly smaller than the experimental values (Fig. 2e). However, the variation trend of the calculated bandgap for the $ZrS_{2(1-x)}Se_{2x}$ alloys is well consistent with the experimental results, i.e., the presence of the bowing effect. Both the experimental and theoretical results prove the tunability of the bandgap of $ZrS_{2(1-x)}Se_{2x}$ by controlling the alloy composition, offering great flexibility for designing various optoelectronic devices.

To elucidate the origin of the bowing effect, the TDOS and PDOS projected on specific Zr, S, or Se atoms for the $ZrS_{2(1-x)}Se_{2x}$ alloys were calculated using DFT. Fig. 2f–h display the calculated TDOS and PDOS for $ZrS_{2(1-x)}Se_{2x}$ with x = 0.25, 0.50, and 0.75, respectively. The dashed vertical lines refer to the energy reference (Fermi level). As shown in Fig. 2f, the conduction band is mainly attributed to the Zr contribution, whereas the valence band is predominantly contributed by both anion atoms of S and Se. Qualitatively, these features are also observed for ZrSSe and $ZrS_{0.5}Se_{1.5}$, as shown in the other two

© Science China Press 2023

panels (Fig. 2g, h). Obviously, two anion atoms (S and Se) compete in trapping electronic charges and contributing to the electronic structure of the valence band, which causes the bandgap bowing effect, as reported previously [41]. Consequently, the bandgap varies quadratically with the Se composition (x).

TEM was utilized to investigate the microstructure and elemental distribution of the as-grown $ZrS_{1.12}Se_{0.88}$ alloys. Fig. 3a shows a high-angle annular dark-field scanning TEM (HAADF-STEM) image of the $ZrS_{1.12}Se_{0.88}$ alloy and the corresponding EDS elemental mapping of Zr, S, and Se, which reveals the uniform dispersion of Se and S throughout the entire ternary domain. Moreover, x is calculated from the EDS spectroscopy to be ~0.42 (Fig. 3b), which is consistent with the result from the XPS measurements. Fig. 3c shows a cross-sectional view of the $ZrS_{1.12}Se_{0.88}$ flake, revealing a perfectly layered structure with a 0.598-nm interlayer distance, which is well matched with the c-value determined from the XRD patterns. Fig. 3d shows a typical top-view high-resolution TEM (HRTEM) image of the $ZrS_{1.12}Se_{0.88}$ flake. The enlarged lattice image (Fig. 3e), together with the sharp diffraction spots in the selected area electron diffraction (SAED) pattern (inset of Fig. 3e), demonstrates the high crystallinity of the $ZrS_{1.12}Se_{0.88}$ alloy. The 0.321-nm lattice plane spacing matches well with the (10-10) plane spacing of the $ZrS_{1.12}Se_{0.88}$ alloy based on Vegard's law. The diffraction spots denoted by the yellow and blue circles in the SAED pattern correspond to the {10-10} and {11-20} planes of $ZrS_{1.12}Se_{0.88}$, respectively. The further enlarged HRTEM image (Fig. 3f) is used to identify the distribution of S and Se in the $ZrS_{1.12}Se_{0.88}$ alloy. It shows different brightness levels depending on their atomic numbers, and the brightest spots with a hexagonal structure represent the heaviest Zr atoms. Fig. 3g shows the brightness profile along the red-dashed line in Fig. 3f. The two brightest spots represent Zr atoms due to the highest atomic number of Zr, whereas the medium-brightness and the dimmest spots represent the Se and S atoms, respectively. By carefully analyzing the intensity of these spots, the Zr, Se, and S atoms are schematically illustrated by purple, blue and red spheres (inset of Fig. 3f). Clearly, it shows a characteristic of the 1T phase structure and the S and Se atoms are randomly distributed within the lattice of alloy.

To explore the optoelectronic properties and potential applications of $ZrS_{2(1-x)}Se_{2x}$ alloys, three alloy films ($ZrS_{1.62}Se_{0.38}$, $ZrS_{1.12}Se_{0.88}$, and $ZrS_{0.48}Se_{1.52}$) were used to fabricate photodetectors which comprise two 200-nm-thick Au electrodes (Fig. S8). Fig. 4a–c show the semilogarithmic I-V curves in the dark and under the 405-nm laser illumination with various power densities. When x increases from 0.19 to 0.76, the dark current at 10 V increases from ~7×10^{-3} to ~3×10^{-2} nA, and the photocurrent under a power density of 125 mW cm^{-2} decreases from ~3×10^{2} to 4 nA. The increased dark current is due to the fact that more defects are present in the $ZrS_{2(1-x)}Se_{2x}$ alloys with higher Se contents, whereas the reduced photocurrent is attributed to the decreased light absorption of the $ZrS_{2(1-x)}Se_{2x}$ alloys as x increases (Fig. S9).

The light on-off ratio of the $ZrS_{2(1-x)}Se_{2x}$-based photodetector,

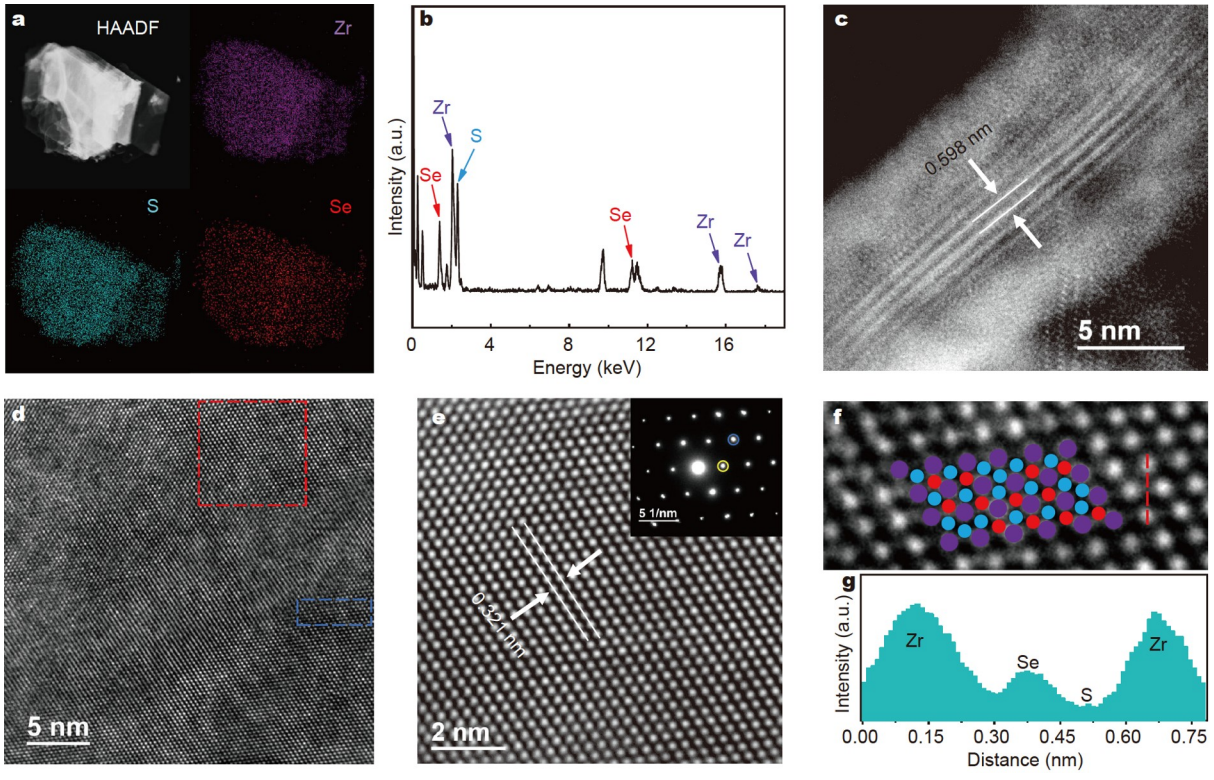

Figure 3 (a) HAADF-STEM image of $ZrS_{1.12}Se_{0.88}$ and the corresponding EDS elemental mapping of Zr, S, and Se atoms. (b) EDS spectrum of $ZrS_{1.12}Se_{0.88}$. (c) Cross-sectional- and (d) top-view HRTEM images of $ZrS_{1.12}Se_{0.88}$ flake, revealing a clear layered structure and perfect crystallinity. (e) Enlarged lattice image of the red-dashed box area in panel (d). The inset shows the corresponding SAED pattern, and the diffraction spots denoted by the yellow and blue circles correspond to the {10-10} and {11-20} planes of $ZrS_{1.12}Se_{0.88}$. (f) Further enlarged HRTEM image of the blue dashed box area in panel (d). The inset shows the distribution of Zr (purple spheres), S (blue spheres), and Se (red spheres). (g) Intensity profile along the red-dashed line in panel (f), indicating the occupancies of Zr, Se, and S atoms.

© Science China Press 2023

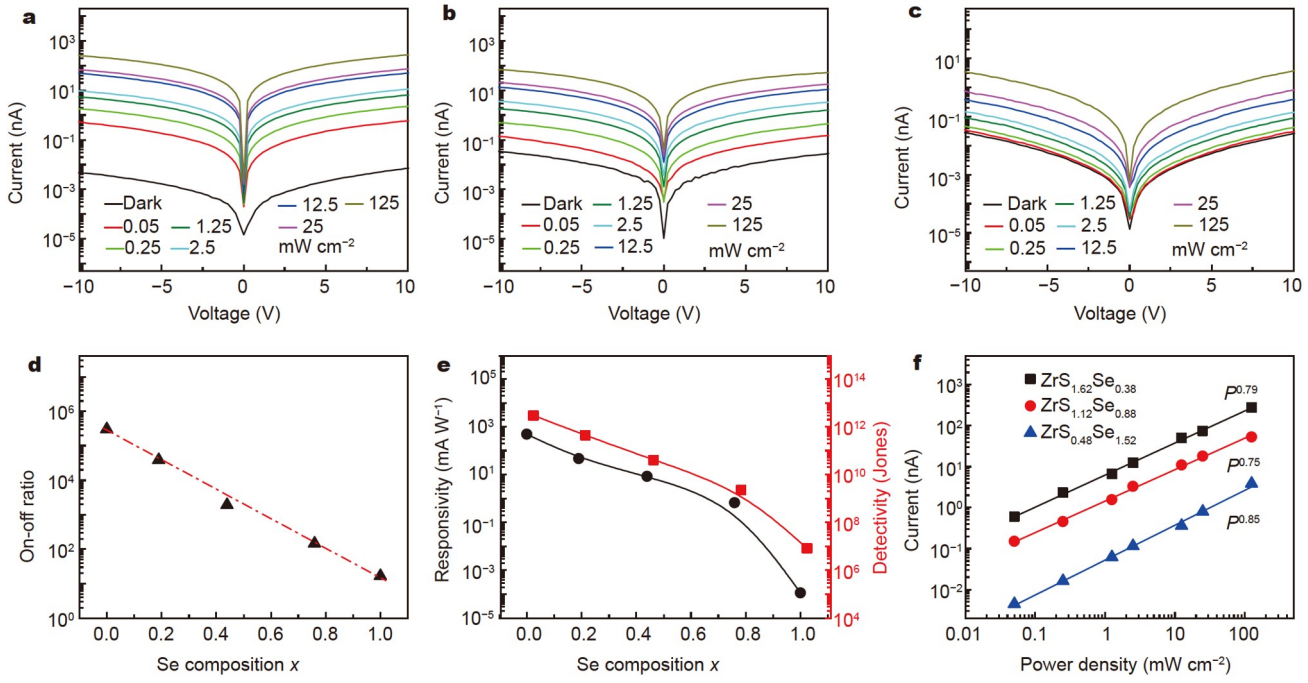

Figure 4 Semilogarithmic *I-V* curves of (a) $ZrS_{1.62}Se_{0.38}$-, (b) $ZrS_{1.12}Se_{0.88}$-, and (c) $ZrS_{0.48}Se_{1.52}$-based photodetectors in the dark and under the 405-nm laser with various power densities. (d) Light on-off ratio obtained with a power density of 125 mW cm^{-2} at 10 V as a function of the Se composition (x). (e) Dependence of responsivity (R) and specific detectivity (D^*) on the Se composition (x). The lines are only for eye-guide. (f) Photocurrents (I_{ph}) of $ZrS_{2(1-x)}Se_{2x}$ photodetectors at 10 V as a function of the illumination power density (P). The data are fitted by a power law $I_{ph} \propto P^{\theta}$.

calculated with a power density of 125 mW cm^{-2} at 10 V, is plotted as a function of x in Fig. 4d. When x increases from 0 to 1, the light on-off ratio distinctly decreases from ~3 × 10^5 to 20, indicating the weaker light response-ability for the photodetectors with higher x-values. Fig. 4e shows the dependence of responsivity (R) and specific detectivity (D^*) on the Se composition x. Evidently, R is remarkably reduced from 490 to 1.13 × 10^{-4} mA W^{-1}, whereas D^* decreases from 3.0 × 10^{12} to 8.22 × 10^6 Jones, as x increases from 0 to 1. Obviously, the device performances, such as the light on-off ratio, responsivity, and specific detectivity, are significantly improved as x decreases. The ZrS_2-based photodetector exhibits the best performance, which is superior to most photodetectors fabricated from other group-IVB TMDs [31,32,34,42,43].

Fig. 4f shows the photocurrent (I_{ph}) of the $ZrS_{2(1-x)}Se_{2x}$ photodetector at 10 V as a function of the laser power density P. Clearly, the I_{ph} monotonically increases as the power density (P) increases for all three photodetectors, indicating that the photoresponse is mostly determined by photocarriers [21]. The relationship between I_{ph} and P can be fitted by a power law $I_{ph} \propto P^{\theta}$. The fitting parameter (θ) is determined to be 0.79, 0.75, and 0.85 for the $ZrS_{2(1-x)}Se_{2x}$ photodetectors with x = 0.19, 0.44, and 0.76, respectively, which is comparable to that of some layered TMD photodetectors [44,45]. In contrast, the photodetectors based on the binary ZrS_2 and $ZrSe_2$ films show a near-linear $I_{ph} \propto P$ relationship [32,33]. The sublinear feature of the $I_{ph} \propto P$ relationship observed herein indicates the presence of numerous defects and traps in the ternary alloys, especially in the $ZrS_{2(1-x)}Se_{2x}$ alloy with a middle Se composition. Therefore, we propose that the traps and defects in $ZrS_{2(1-x)}Se_{2x}$ alloys are mainly associated with the alloying disorder.

Fig. 5a shows the normalized spectral photoresponse curves for four $ZrS_{2(1-x)}Se_{2x}$-based photodetectors measured at 10 V using a xenon lamp-monochromator combination. The evident photoresponse is observed within the visible light range for all four devices, whereas the photoresponse edge shifts toward longer wavelength as x increases. The cutoff wavelengths are determined to be 720, 800, 950, and 1050 nm (corresponding to 1.72, 1.55, 1.31, and 1.18 eV) for the $ZrS_{1.62}Se_{0.38}$, $ZrS_{1.38}Se_{0.62}$, $ZrS_{0.78}Se_{1.22}$, and $ZrS_{0.48}Se_{1.52}$ photodetectors, respectively. These values are very close to their bandgaps (1.71, 1.52, 1.30, and 1.15 eV) estimated from the UV-Vis absorption spectra (Fig. S10). Furthermore, the rapid increase in photoresponse is observed at wavelengths of 578, 618, 700, and 735 nm (corresponding to 2.15, 2.01, 1.77, and 1.69 eV) for the $ZrS_{1.62}Se_{0.38}$, $ZrS_{1.38}Se_{0.62}$, $ZrS_{0.78}Se_{1.22}$, and $ZrS_{0.48}Se_{1.52}$ photodetectors, respectively, which is attributed to the high light absorption at the minimum direct band gap. Different spectral response bands are achieved depending on the alloy composition, which will greatly expand the applications of Zr-based TMDs in optoelectronics.

Fig. 5b shows the photo-switching behavior of the $ZrS_{2(1-x)}Se_{2x}$-based photodetectors measured under periodic on-off laser irradiation with a power density of 25 mW cm^{-2}. All photodetectors display a highly stable and repeatable photoresponse to the 405-nm light illumination over several cycles. To obtain the response time of detectors, the current-time (*I-t*) curves were recorded under a 405-nm light illumination using an oscilloscope. As shown in Fig. S11, the rise and decay times are determined to be ~95/165, 110/280, and 90/115 μs for the $ZrS_{1.62}Se_{0.38}$, $ZrS_{1.12}Se_{0.88}$, and $ZrS_{0.48}Se_{1.52}$ photodetectors, respectively. They are two orders of magnitude faster than those of the $MoS_{2(1-x)}Se_{2x}$-based [46] and $ReS_{2(1-x)}Se_{2x}$-based [21] photodetectors and superior to most reported group-IVB TMD-

© Science China Press 2023

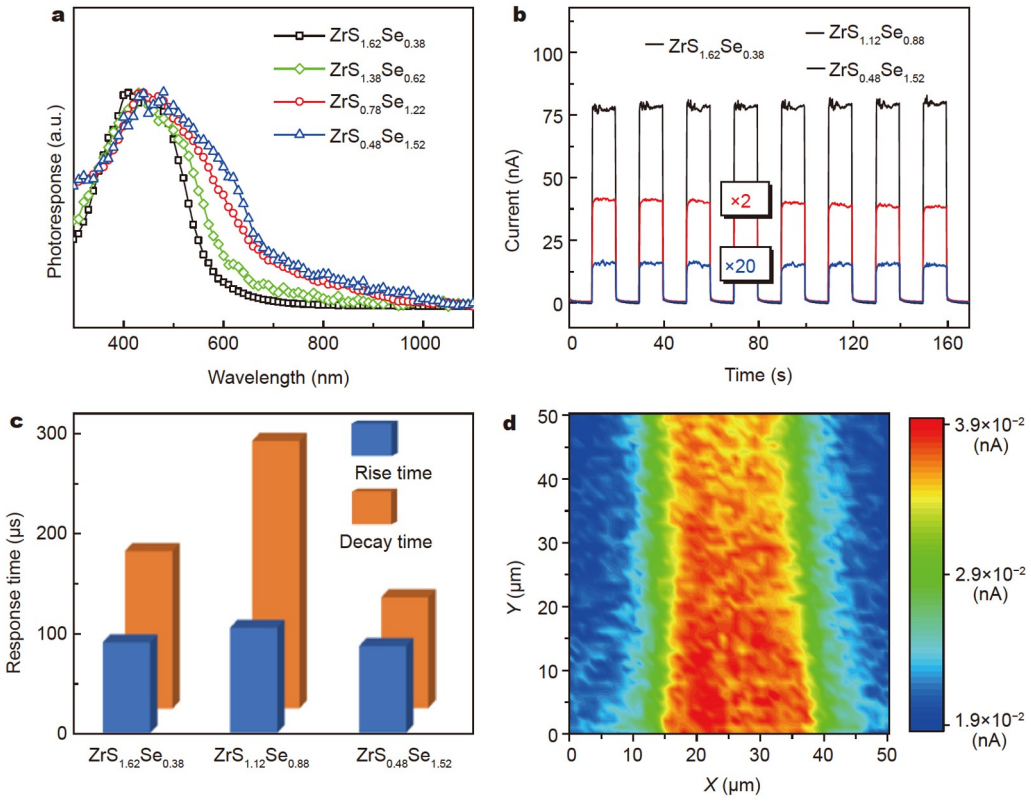

Figure 5 (a) Normalized spectral photoresponse curves measured at 10 V for four $ZrS_{2(1-x)}Se_{2x}$-based photodetectors with different *x*-values; (b) photoswitching behavior of $ZrS_{2(1-x)}Se_{2x}$-based photodetectors measured under the 405-nm laser with a power density of 25 mW cm^{-2} at 10 V; (c) rise and decay times of $ZrS_{1.62}Se_{0.38}$, $ZrS_{1.12}Se_{0.88}$, and $ZrS_{0.48}Se_{1.52}$ photodetectors; (d) photocurrent mapping of $ZrS_{1.62}Se_{0.38}$-based photodetectors under 405-nm laser illumination.

based photodetectors [31,34,42,43,47]. Fig. 5c compares the response times and *x*. The slightly increased rise and decay times for the $ZrS_{1.12}Se_{0.88}$ photodetector may be related to the reduced mobility because of the larger alloy scattering for the middle Se composition alloy. To identify the spatial distribution of the photocurrent, the photocurrent mapping of the $ZrS_{1.62}Se_{0.38}$-based photodetector was measured under 405-nm laser illumination. The scan area is 50 μm × 50 μm, and the diameter of the laser spot is ~1 μm. As shown in Fig. 5d, the entire channel area (20 μm × 50 μm) confined between two Au electrodes is photoactive, and the photocurrent distribution is rather uniform with a small relative standard deviation of ±12%.

CONCLUSIONS

Herein, we have demonstrated that large-area $ZrS_{2(1-x)}Se_{2x}$ alloys with fully tunable chemical compositions can be epitaxially grown on *c*-plane sapphire substrates *via* a facile single-step CVD method. The TMD alloys show progressive variations in their XRD, Raman, and UV-Vis absorption spectra, corresponding with the Se composition. HRTEM characterizations confirm their single-crystalline structure with uniform alloying elements. Especially, both the UV-Vis spectra and DFT calculations indicate that the bandgap of the alloys exhibits a pronounced bowing behavior with continuously tunable bandgaps from 1.86 to 1.15 eV depending on the Se composition. The $ZrS_{2(1-x)}Se_{2x}$-based photodetectors demonstrate a sensitive photoresponse to visible light with a fast response time of ~100 μs. Besides, their performances such as the light on-off ratio, responsivity, and specific detectivity, are significantly improved as the Se composition decreases. Overall, this work provides an efficient way to obtain TMD alloys with tunable optoelectronic properties and opens up the possibility of creating unprecedented applications.

Received 14 September 2022; accepted 21 October 2022; published online 17 January 2023

1 Li H, Li Y, Aljarb A, *et al.* Epitaxial growth of two-dimensional layered transition-metal dichalcogenides: Growth mechanism, controllability, and scalability. Chem Rev, 2018, 118: 6134–6150
2 Wang X, Song Z, Wen W, *et al.* Potential 2D materials with phase transitions: Structure, synthesis, and device applications. Adv Mater, 2019, 31: 1804682
3 Zhou J, Lin J, Huang X, *et al.* A library of atomically thin metal chalcogenides. Nature, 2018, 556: 355–359
4 Wu M, Xiao Y, Zeng Y, *et al.* Synthesis of two-dimensional transition metal dichalcogenides for electronics and optoelectronics. InfoMat, 2021, 3: 362–396
5 Lin YC, Torsi R, Geohegan DB, *et al.* Controllable thin-film approaches for doping and alloying transition metal dichalcogenides monolayers. Adv Sci, 2021, 8: 2004249
6 Yao J, Yang G. 2D layered material alloys: Synthesis and application in electronic and optoelectronic devices. Adv Sci, 2022, 9: 2103036
7 Li H, Duan X, Wu X, *et al.* Growth of alloy $MoS_{2x}Se_{2(1-x)}$ nanosheets with fully tunable chemical compositions and optical properties. J Am Chem Soc, 2014, 136: 3756–3759
8 Feng Q, Zhu Y, Hong J, *et al.* Growth of large-area 2D $MoS_{2(1-x)}Se_{2x}$ semiconductor alloys. Adv Mater, 2014, 26: 2648–2653
9 Lim YR, Han JK, Yoon Y, *et al.* Atomic-level customization of 4 in.

 © Science China Press 2023

transition metal dichalcogenide multilayer alloys for industrial applications. Adv Mater, 2019, 31: 1901405
10 Fu Q, Yang L, Wang W, *et al.* Synthesis and enhanced electrochemical catalytic performance of monolayer $WS_{2(1-x)}Se_{2x}$ with a tunable band gap. Adv Mater, 2015, 27: 4732–4738
11 Duan X, Wang C, Fan Z, *et al.* Synthesis of $WS_{2x}Se_{2-2x}$ alloy nanosheets with composition-tunable electronic properties. Nano Lett, 2016, 16: 264–269
12 Sun H, Zhou X, Wang X, *et al.* p-n conversion of charge carrier types and high photoresponsive performance of composition modulated ternary alloy $W(S_xSe_{1-x})_2$ field-effect transistors. Nanoscale, 2020, 12: 15304–15317
13 Apte A, Krishnamoorthy A, Hachtel JA, *et al.* Telluride-based atomically thin layers of ternary two-dimensional transition metal dichalcogenide alloys. Chem Mater, 2018, 30: 7262–7268
14 Yu P, Lin J, Sun L, *et al.* Metal-semiconductor phase-transition in $WSe_{2(1-x)}Te_{2x}$ monolayer. Adv Mater, 2017, 29: 1603991
15 Song JG, Ryu GH, Lee SJ, *et al.* Controllable synthesis of molybdenum tungsten disulfide alloy for vertically composition-controlled multilayer. Nat Commun, 2015, 6: 7817
16 Liu X, Wu J, Yu W, *et al.* Monolayer $W_xMo_{1-x}S_2$ grown by atmospheric pressure chemical vapor deposition: Bandgap engineering and field effect transistors. Adv Funct Mater, 2017, 27: 1606469
17 Yu H, Yan H, Li H, *et al.* Spatially graded millimeter sized $Mo_{1-x}W_xS_2$ monolayer alloys: Synthesis and memory effect. ACS Appl Mater Interfaces, 2021, 13: 44693–44702
18 Kim J, Seung H, Kang D, *et al.* Wafer-scale production of transition metal dichalcogenides and alloy monolayers by nanocrystal conversion for large-scale ultrathin flexible electronics. Nano Lett, 2021, 21: 9153–9163
19 Li X, Lin MW, Basile L, *et al.* Isoelectronic tungsten doping in monolayer $MoSe_2$ for carrier type modulation. Adv Mater, 2016, 28: 8240–8247
20 Cui F, Feng Q, Hong J, *et al.* Synthesis of large-size 1T′ $ReS_{2x}Se_{2(1-x)}$ alloy monolayer with tunable bandgap and carrier type. Adv Mater, 2017, 29: 1705015
21 Kang P, Nan H, Zhang X, *et al.* Controllable synthesis of crystalline $ReS_{2(1-x)}Se_{2x}$ monolayers on amorphous SiO_2/Si substrates with fast photoresponse. Adv Opt Mater, 2020, 8: 1901415
22 Wang Z, Zhao X, Yang Y, *et al.* Phase-controlled synthesis of monolayer $W_{1-x}Re_xS_2$ alloy with improved photoresponse performance. Small, 2020, 16: 2000852
23 An B, Ma Y, Chu F, *et al.* Growth of centimeter scale $Nb_{1-x}W_xSe_2$ monolayer film by promoter assisted liquid phase chemical vapor deposition. Nano Res, 2022, 15: 2608–2615
24 Zuo Y, Liu C, Ding L, *et al.* Robust growth of two-dimensional metal dichalcogenides and their alloys by active chalcogen monomer supply. Nat Commun, 2022, 13: 1007
25 Yan C, Gong C, Wangyang P, *et al.* 2D group IVB transition metal dichalcogenides. Adv Funct Mater, 2018, 28: 1803305
26 Zhang W, Huang Z, Zhang W, *et al.* Two-dimensional semiconductors with possible high room temperature mobility. Nano Res, 2014, 7: 1731–1737
27 Fiori G, Bonaccorso F, Iannaccone G, *et al.* Electronics based on two-dimensional materials. Nat Nanotech, 2014, 9: 768–779
28 Oliver SM, Fox JJ, Hashemi A, *et al.* Phonons and excitons in $ZrSe_2$-ZrS_2 alloys. J Mater Chem C, 2020, 8: 5732–5743
29 Fox JJ, Bachu S, Cavalero RL, *et al.* Chemical vapor transport synthesis, characterization and compositional tuning of ZrS_xSe_{2-x} for optoelectronic applications. J Cryst Growth, 2020, 542: 125609
30 Moustafa M, Paulheim A, Mohamed M, *et al.* Angle-resolved photoemission studies of the valence bands of ZrS_xSe_{2-x}. Appl Surf Sci, 2016, 366: 397–403
31 Wang D, Zhang X, Guo G, *et al.* Large-area synthesis of layered $HfS_{2(1-x)}Se_{2x}$ alloys with fully tunable chemical compositions and bandgaps. Adv Mater, 2018, 30: 1803285
32 Tian Y, Zheng M, Cheng Y, *et al.* Epitaxial growth of $ZrSe_2$ nanosheets on sapphire *via* chemical vapor deposition for optoelectronic application. J Mater Chem C, 2021, 9: 13954–13962
33 Tian Y, Cheng Y, Huang J, *et al.* Epitaxial growth of large area ZrS_2 2D semiconductor films on sapphire for optoelectronics. Nano Res, 2022, 15: 6628–6635
34 Mattinen M, Popov G, Vehkamäki M, *et al.* Atomic layer deposition of emerging 2D semiconductors, HfS_2 and ZrS_2, for optoelectronics. Chem Mater, 2019, 31: 5713–5724
35 Mañas-Valero S, García-López V, Cantarero A, *et al.* Raman spectra of ZrS_2 and $ZrSe_2$ from bulk to atomically thin layers. Appl Sci, 2016, 6: 264
36 Jadczak J, Dumcenco DO, Huang YS, *et al.* Composition dependent lattice dynamics in $MoS_xSe_{(2-x)}$ alloys. J Appl Phys, 2014, 116: 193505
37 Wang Z, Liu P, Ito Y, *et al.* Chemical vapor deposition of monolayer $Mo_{1-x}W_xS_2$ crystals with tunable band gaps. Sci Rep, 2016, 6: 21536
38 Ghafari A, Boochani A, Janowitz C, *et al.* Electronic structure of ZrS_xSe_{2-x} by Tran-Blaha modified Becke-Johnson density functional. Phys Rev B, 2011, 84: 125205
39 Ghafari A, Janowitz C. Electronic and thermoelectric properties of ZrS_xSe_{2-x}. Comput Mater Sci, 2019, 169: 109109
40 Lebègue S, Eriksson O. Electronic structure of two-dimensional crystals from *ab initio* theory. Phys Rev B, 2009, 79: 115409
41 Alfalasi W, Al Qasir I, Tit N. Origins of bandgap bowing character in the common-anion transition-metal-dichalcogenide ternary alloyed monolayer: *Ab initio* investigation. New J Phys, 2021, 23: 103027
42 Wang D, Meng J, Zhang X, *et al.* Selective direct growth of atomic layered HfS_2 on hexagonal boron nitride for high performance photodetectors. Chem Mater, 2018, 30: 3819–3826
43 Yan C, Gan L, Zhou X, *et al.* Space-confined chemical vapor deposition synthesis of ultrathin HfS_2 flakes for optoelectronic application. Adv Funct Mater, 2017, 27: 1702918
44 Mo H, Zhang X, Liu Y, *et al.* Two-dimensional alloying molybdenum tin disulfide monolayers with fast photoresponse. ACS Appl Mater Interfaces, 2019, 11: 39077–39087
45 Yu J, Xu CY, Li Y, *et al.* Ternary $SnS_{2-x}Se_x$ alloys nanosheets and nanosheet assemblies with tunable chemical compositions and band gaps for photodetector applications. Sci Rep, 2015, 5: 17109
46 Zhang J, Qian Y, Nan H, *et al.* Large-scale $MoS_{2(1-x)}Se_{2x}$ monolayers synthesized by confined-space CVD. Nanotechnology, 2021, 32: 355601
47 Zheng B, Chen Y, Wang Z, *et al.* Vertically oriented few-layered HfS_2 nanosheets: Growth mechanism and optical properties. 2D Mater, 2016, 3: 035024

Acknowledgements This work was supported by the National Natural Science Foundation of China (61874106 and 62274151) and the Strategic Priority Research Program of the Chinese Academy of Sciences (XDB43000000).

Author contributions Huang J, Li X, and Zhang X conceived and designed the project and wrote the manuscript. Huang J and Tian Y prepared the samples and performed the experiments; Chen J and Zhang S participated in the investigation; Cheng Y and Yin Z performed the DFT calculations; Li J, Jiang J, and Wang G participated in the analysis of the data; Zhang X supervised the project; all authors contributed to the general discussion. All authors read and approved the manuscript.

Conflict of interest The authors declare that they have no conflict of interest.

Supplementary information Supporting data are available in the online version of the paper.

© Science China Press 2023



Jidong Huang received his BEng degree from the College of Physics, Qingdao University. He is a Master's degree candidate under the supervision of Prof. Xingwang Zhang. His research interest focuses on 2D materials and their applications.



Xingxing Li received his Master's degree from Hubei University in 2016 and PhD degree from the University of Chinese Academy of Sciences in 2019. He joined the Faculty of Intelligent Manufacturing, Wuyi University in 2019. His research focuses on oxide thin films, 2D materials, and semiconductor devices.



Xingwang Zhang is a full professor at the Institute of Semiconductors, Chinese Academy of Sciences. He received his BSc and PhD degrees from Lanzhou University in 1994 and 1999, respectively. Afterward, he worked as a postdoctoral fellow at The Chinese University of Hong Kong from 1999 to 2001. Then, he worked as a Humboldt research fellow at the University of Ulm, Germany, from 2001 to 2004. His current research interests include ultrawide bandgap semiconductors, 2D materials, and photovoltaic materials and devices.

全组分/带隙可调的二维$ZrS_{2(1-x)}Se_{2x}$半导体合金的外延生长及其光电应用

黄吉东[1,2], 田琰[1,2], 程勇[1,2], 李星星[3*], 张丝雨[1,2], 江季[1,2], 陈镜壬[1,2], 王高凯[1,2], 李景祯[1,2], 尹志岗[1,2], 张兴旺[1,2,3*]

摘要 过渡金属硫化物(TMDs)的带隙工程对于拓宽其在电子和光电子器件中的应用具有重要意义. 本文中, 我们首次报道了通过简单的一步化学气相沉积法在蓝宝石衬底上外延生长大面积、全组分可调的$ZrS_{2(1-x)}Se_{2x}$合金薄膜. $ZrS_{2(1-x)}Se_{2x}$合金表现出优异的单晶性和外延质量, 以及均匀的元素分布, 其与衬底的外延关系被确定为$ZrS_{2(1-x)}Se_{2x}$(0001)[10-10]//蓝宝石(0001)[11-20]. $ZrS_{2(1-x)}Se_{2x}$合金的带隙随组分的变化从1.86到1.15 eV连续可调, 且表现出明显的弯曲特性. 基于$ZrS_{2(1-x)}Se_{2x}$的光电探测器对可见光具有灵敏的光响应, 响应时间约为100 μs, 随着Se组分的减少, 探测器性能显著提高. 本工作为合成带隙可调的$ZrS_{2(1-x)}Se_{2x}$合金提供了一种有效方法, 为设计基于TMDs的光电器件提供了极大的灵活性.

© Science China Press 2023